



# Effect of Tension Temperature on the Anisotropy of Tensile Behavior for Az31 Alloys: A Visco-Plastic Self-Consistent Analysis

Wenke Wang<sup>1</sup> · Jaimyun Jung<sup>4</sup> · Chao Cui<sup>1</sup> · Wenzhen Chen<sup>1</sup> · Yang Yu<sup>1</sup> · Peng Li<sup>1</sup> · Wencong Zhang<sup>1</sup> · Renlong Xiong<sup>3</sup> · Hyoung Seop Kim<sup>2</sup>

Received: 9 May 2022 / Accepted: 1 July 2022 / Published online: 27 July 2022  
© The Author(s) under exclusive licence to The Korean Institute of Metals and Materials 2022

## Abstract

In this work, the anisotropy variation of tensile flow stress for AZ31 magnesium alloys was investigated at various temperatures and tensile strains with the help of the visco-plastic self-consistent model. The results showed that the anisotropy of flow stress was weakened with the increase of tensile temperature, while such anisotropy presented a slightly increasing stage first and then a continuously decreasing stage with the increase of tensile strain. During the tension deformation, the activations of basal slip and tension twinning, together contributed to the development of a (0002)//LD (LD: loading direction) type texture. In contrast, the activations of prismatic slip produced a  $\langle 10\text{--}10 \rangle$ //LD type texture. Such texture variations influenced the Taylor factors, but did not cause significant differences in the flow stress. By comparison, the difference in the macroscopic average resolved shear stress, which was calculated according to the critical resolved shear stress of each deformation mode and their respective activation fractions, decreased significantly with the increase of tensile temperature or tensile strain. This was the major reason for the decline of the tension deformation behavior anisotropy.

**Keywords** Tension deformation behavior · Anisotropy variations · Deformation mode · Texture · Visco-plastic self-consistent model (VPSC) model

## 1 Introduction

Wrought magnesium alloys have attracted significant attention in the aerospace and automotive industries where light weight is critical [1–3]. However, owing to the inherent hexagonal close-packed (HCP) structure, wrought magnesium alloys usually possess a strong basal texture, which produces

significant anisotropy of plastic deformation at room temperature. This is undesirable both for achieving good formability and for use in some critical engineering applications. These have severely restricted the widespread commercial use of such alloys [4–7].

For the magnesium alloys, the above anisotropy is closely related to their deformation modes [8, 9]. At room temperature, the critical resolved shear stresses (CRSS) of non-basal slips (prismatic or pyramidal slips) are much higher than that of basal slip [3, 10, 11]. For example, the CRSS reached 90–150 MPa for non-basal slip while it was only 5–20 MPa for basal slip [10, 12, 13]. Nevertheless, the non-basal slips still needed to be activated during plastic deformation because the single basal slip activation could not accommodate the c-axis strain [4, 11]. To activate these non-basal slips, the external stresses needed to be high enough to produce plastic deformation, consequently exhibiting higher flow stress. Such high stress decreased with the contribution increase of basal slip. Typically, in the study of Agnew et al., the yield stress decreased by half owing to the increase of basal slip activation when the basal poles were rotated

✉ Hyoung Seop Kim  
hskim@postech.ac.kr

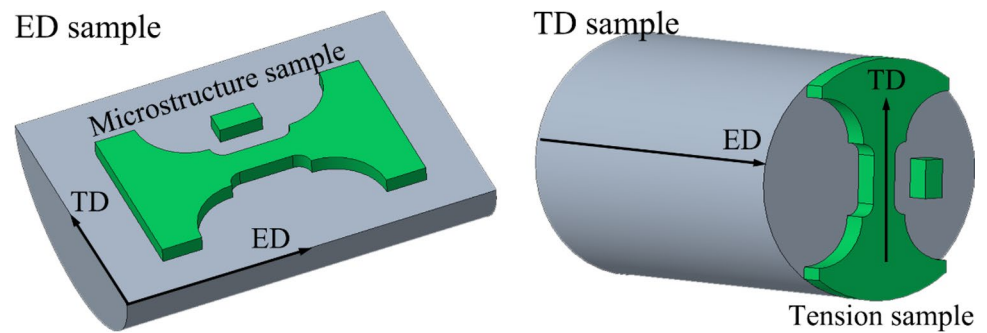
<sup>1</sup> School of Materials Science and Engineering, Harbin Institute of Technology, Weihai 264209, People's Republic of China

<sup>2</sup> Graduate Institute of Ferrous & Energy Materials Technology (GIFT), Pohang University of Science and Technology, Pohang 37673, Republic of Korea

<sup>3</sup> School of Mechanical and Electrical Engineering, Wuhan Institute of Technology, Wuhan 430205, People's Republic of China

<sup>4</sup> Department of Materials AI & Big-Data, Korea Institute of Materials Science (KIMS), Changwon 51508, Republic of Korea

**Fig. 1** Schematic illustration of sampling strategy for the ED samples and the TD samples



away from the normal direction (ND) to approximately 45° [14]. Actually, the tension twinning in magnesium alloys could also accommodate the *c*-axis strain [8]. This meant that the activation of tension twinning could replace non-basal slips to relieve the complicated deformation strain. Importantly, the lower CRSS of tension twinning, similar in magnitude to that of basal slip, made them activated much easier than the non-basal slips, thereby presenting a much lower flow stress [4, 11]. This resulted in the significant anisotropy of flow stress.

With regard to the above anisotropy, our previous work once showed that the anisotropy of yield stress in a ZK60 magnesium alloy sheet decreased at the elevated deformation temperature. This was attributed to the decline of CRSS difference between the non-basal slips and the basal slips [15]. However, such influence mechanisms were not analyzed quantitatively in that work, especially the contribution of each deformation mode to the total strain. In addition, that work solely considered the anisotropy about the yield stress instead of the entire tension deformation behavior [15]. In this regard, Wang et al. attributed the remarkable decline of yield stress to the variation in the dominant deformation modes from the basal slip and prismatic slip to the tension twinning [28]. Jiang et al. obtained a similar trend that the anisotropic degree of yield stress was minimized to 10 MPa from 125 MPa when the tension deformation was along different directions [33]. In fact, the continuous plastic deformation would ceaselessly rotate the grain lattice, significantly influencing the Schmid factor of each deformation mode. As a result, the contributions of slip or twinning systems to the total strain varied greatly over the entire tension deformation [16]. Such variations severely influenced the microstructure states and the plastic deformation behaviors, causing remarkable dynamic variation in the anisotropy. Additionally, the sensitivity of the CRSS of each deformation mode to the deformation temperature also influenced the above anisotropy. The point was that such anisotropy variations were deemed to be more important in the forming-technology design, especially for the prevalent warm-forming condition of magnesium alloy sheets. Moreover, the dominant mechanism for the dramatic anisotropy

variation caused by the deformation strain or temperature was not clear.

Therefore, this work focused on the anisotropy variations during the entire tension deformation under various deformation temperatures. Meanwhile, the visco-plastic self-consistent model (VPSC) was used to quantify the contribution of each deformation mode to the macroscopic strain.

## 2 Experimental and Modeling Details

### 2.1 Experimental Procedure and Characterization

The initial material used in this work was the as-extruded Mg-3.0 wt%Al-1.0 wt%Zn alloy (AZ31 magnesium alloy). Prior to the tension deformation, the initial material was subjected to heat treatment at 200 °C for 60 min to eliminate the residual stress. As shown in Fig. 1, the tension samples and the transverse tension samples were machined along the ED and the TD from an AZ31 magnesium alloy rod, respectively. The gauges in these tension samples were 5 mm long, 2.5 mm wide, and 2 mm thick. Uniaxial tension tests were carried out using an MTS electronic universal testing machine at an initial strain rate of  $1.0 \times 10^{-3} \text{ s}^{-1}$  under various deformation temperatures (20, 100, and 200 °C). In this work, the maximum deformation temperature was selected as 200 °C based on the following considerations. First, in order to reduce energy consumption and improve productivity, the warm-forming condition of magnesium alloy sheets was the industrialization goal in which the forming temperature was generally below 200 °C. Second, much literature reported that there still existed the obvious texture effect on the anisotropy of flow stress under the deformation temperature of 200 °C [15, 34]. Therefore, this work selected 200 °C as the maximum deformation temperature. Before the tension test, the samples were heated at the target temperature for 10 min to ensure consistent temperature in the entire sample. After the tension tests, the samples were water-quenched to room temperature so as to preserve the as-deformed microstructures. During the tension test, the engineering stress–strain data was recorded, and subsequently numerically computed to obtain the true stress logarithmic

plastic-strain curve. Additionally, both the ED tension tests and the TD tension tests were interrupted at the logarithmic plastic strain of 0.1 and 0.2. These were then used to analyze the microstructure evolution. As shown in Fig. 3a and c, the interruption samples were labeled ED20-A, ED20-B, ED200-A, and ED200-B for the ED samples and TD20-A, TD20-B, TD200-A, and TD200-B for the TD samples. Three samples for each condition were produced to ensure the repeatability of the results.

As shown in Fig. 1, the ED-TD plane and the TD-TD plane microstructure observation samples were used together to characterize the microstructure features and texture states of the initial material. For the interruption tension samples, the microstructure observation cross-sections were cut in the central regions along the loading direction (LD). These microstructure samples were prepared using soft-diamond polishing, followed by electropolishing in a 5:3 solution of C<sub>2</sub>H<sub>5</sub>OH and H<sub>3</sub>PO<sub>4</sub> for 8 min at 0.25 A. Subsequently, their grain morphology and crystallographic texture were examined using electron backscatter diffraction (EBSD) based on scanning electron microscopy (Zeiss). During the EBSD measurement, the accelerating voltage, working distance and sample tilt angle were 20 keV, 15 mm and 70°, respectively. Moreover, to compare the texture evolution conveniently, the texture states on the TD-TD plane in the TD samples were transferred to the ED-TD plane via the rotation function of the reference frame in the OIM software.

## 2.2 Visco-Plastic Self-Consistent Model

The visco-plastic self-consistent (VPSC) model was employed to predict the texture evolution and deformation mode activation of AZ31 magnesium alloy during tension deformation. This model was originally proposed by Molinari and further developed by Lebensohn and Tomé [17–19]. The VPSC model applied a non-linear rate-sensitivity equation to describe the visco-plastic constitutive behavior at grain level [20]. The strain rate in an individual grain was expressed by summing all the shear rates of slip or twinning systems within the grain, as indicated in Eq. 1.

$$\dot{\epsilon}_{ij} = \sum_s m_{ij}^s \dot{\gamma}^s = \dot{\gamma}^0 \sum_s m_{ij}^s \left( \frac{m_{kl}^s : \sigma_{kl}^s}{\tau^{cs}} \right)^n, \quad (1)$$

where  $m_{ij}^s$  and  $\dot{\gamma}^s$  were the symmetric Schmid factor and the shear rate of the deformation mode  $s$ , respectively. The exponent  $n$  was the inverse strain-rate sensitivity and was generally 20 for HCP materials according to the VPSC manual. The term  $\dot{\gamma}^0$  was the normalized shear rate and was set to the macroscopic strain rate of  $1.0 \times 10^{-3} \text{ s}^{-1}$ . Here,  $\sigma_{kl}^s$  and  $\tau^{cs}$  were the stress tensor and the threshold shear stress of the deformation modes, respectively. The evolution of  $\tau^{cs}$  was

associated with the hardening process and was expressed as indicated in Eq. 2.

$$\dot{\tau}^{cs} = \frac{d\hat{\tau}^s}{d\gamma^{ac}} \sum_{\beta} h^{\alpha\beta} \dot{\gamma}^{\beta}, \quad (2)$$

where  $\gamma^{ac} = \sum |\gamma^s|$  was the accumulated shear strain in the grain, and  $h^{\alpha\beta}$  was the latent hardening coupling coefficient representing the obstacles on system  $s$  from system  $\beta$ . The term  $\hat{\tau}^s$  was the CRSS on the specific slip or twinning system based on Voce hardening and was described in other work [5, 20, 21], as indicated in Eq. 3.

$$\hat{\tau}^s = \tau^{0s} + (\tau^{1s} + h^{1s} \gamma^{ac}) \left( 1 - e^{\left( -\frac{h^{0s}}{\tau^{1s}} \gamma^{ac} \right)} \right), \quad (3)$$

where  $\tau^{0s}$  and  $\tau^{0s} + \tau^{1s}$  were the initial CRSS and the back-extrapolated CRSS, respectively, while  $h^{0s}$  and  $h^{1s}$  were the initial hardening rate and the asymptotic hardening rate, respectively. In addition, the predominant twin reorientation (PTR) scheme was used to account for orientation variations induced by twinning, as was proposed by Tomé [5, 22]. This required recording the shear strain contributed by each twinning system  $t$  and the volume fraction  $V^{t,g}$  within each grain  $g$ . The accumulated twin volume fraction  $V^{\text{acc,mode}}$  was calculated by summing all the twinning systems in the overall grains, in a given twinning mode, as shown in Eqs. 4 and 5.

$$V^{t,g} = \frac{\gamma^{t,g}}{\gamma^0}, \quad (4)$$

$$V^{\text{acc,mode}} = \sum_g \sum_t V^{t,g}. \quad (5)$$

A threshold volume fraction  $V^{\text{th,mode}}$  was defined in Eq. 6.

$$V^{\text{th,mode}} = A^{\text{th1}} + A^{\text{th2}} \frac{V^{\text{eff,mode}}}{V^{\text{acc,mode}}}, \quad (6)$$

where  $A^{\text{th1}}$  and  $A^{\text{th2}}$  are the artificial material constants. In each incremental step, a grain was picked arbitrarily, and the twinning system with the highest accumulated volume fraction was identified. If this twinning system was larger than the threshold  $V^{\text{th,mode}}$ , the grain was rotated, and meanwhile, the effective twin fraction  $V^{\text{eff,mode}}$  and the threshold  $V^{\text{acc,mode}}$  were updated.

In this work, the basal slip, prismatic slip, pyramidal  $\langle c+a \rangle$  slip, and tension twinning were selected as the deformation modes in the VPSC model. Here, the higher CRSS of compression twinning made its contribution to the total strain negligible, and therefore compression twinning was not considered in the VPSC model. The material parameters in the VPSC model were usually obtained

**Table 1** Values of material parameters in the VPSC model (unit: MPa)

Temperature (°C)	Mode	$\tau^{0s}$ , MPa	$\tau^{1s}$ , MPa	$h^{0s}$ , MPa	$h^{1s}$ , MPa	$h^{\alpha\beta}$
20	Basal	15.6	6.0	10.0	3.0	1.0
	Prismatic	134.6	35.1	500.0	40.0	1.0
	Pyramidal	200.0	57.3	1500.0	400.0	1.0
	Ten. twinning	25.0	1.2	2.0	1.0	1.0
100	Basal	14.1	6.2	10.0	3.6	1.0
	Prismatic	110.7	30.1	500.0	35.0	1.0
	Pyramidal	180.0	57.1	1500.0	400.0	1.0
	Ten. twinning	25.0	1.2	2.0	1.0	1.0
200	Basal	12.2	6.3	10.0	1.6	1.0
	Prismatic	65.7	20.1	500.0	15.0	1.0
	Pyramidal	100.0	57.1	1500.0	400.0	1.0
	Ten. twinning	25.0	1.2	2.0	1.0	1.0

by matching the experimental flow curves for the tension tests with the simulated ones. To identify these accurate material parameters, the particle swarm optimization (PSO) method was used in this work to realize the material parameter adjustment for both ED sample and TD sample simultaneously [23]. The input texture details in the VPSC model were calculated from the experimental EBSD data. Besides, according to the literature [31], the  $A^{th1}$  and  $A^{th2}$  for the tension twinning was set to 0.7 and 0.8, respectively. Based on the above settings, the material parameters were identified via the PSO method, as shown in Table 1.

### 3 Results and Discussion

#### 3.1 Initial Microstructure and the True Stress-Logarithmic Plastic Strain Curves

Figure 2 showed the microstructure characteristics of the as-extruded AZ31 magnesium alloy using the inverse pole figure maps on the ED-TD plane and the TD-TD plane. As shown in Fig. 2a, the ED-TD plane sample exhibited a duplex structure with coarse grains surrounded by small equiaxed grains, and its average grain size was about 15.5  $\mu\text{m}$ . The TD-TD plane sample possessed a similar duplex microstructure with an average grain size of about 16.1  $\mu\text{m}$  (Fig. 2b). With regard to the texture state of the initial material, both the (0002) pole figures depicted similar extruded fiber textures in which the c-axes in the vast majority of grains were almost perpendicular to the ED (Fig. 2c, d). Their maximum texture intensities were about 3.4–4.1.

As reported in previous work, the strong mechanical property anisotropy of magnesium alloys at room temperature was ascribed to the nonuniform distribution of basal poles on the rolling plane [15]. To clearly depict the basal

texture difference between the ED and the TD, their (0002) basal pole density distributions were summarized in Fig. 2e. The data processing method could be referred to in our previous work [24, 25]. Clearly, Fig. 2e depicted a large distribution difference of (0002) basal pole density between the ED and the TD. More specifically, the (0002) basal poles in the ED sample were centrally distributed within the angle range of 66°–90° away from the ED, while that in the TD sample was dispersed along the TD. This was consistent with the texture result in the (0002) pole figures.

Figure 3 showed the anisotropy variations of tension deformation behavior between the ED samples and the TD samples at different tensile temperatures. As shown in Fig. 3a, the true stress–logarithmic plastic strain curves at 20 °C depicted obvious anisotropy between the ED sample and the TD sample. The ED sample presented a power-law shape flow stress curve with slow strain hardening behavior after the yield stress of about 212 MPa, while the TD sample exhibited a concave-down-shaped flow-stress curve with relatively quick hardening behavior after the yield stress of 129 MPa. Such strong anisotropy gradually weakened with the increase of tensile temperature according to the curve results in Fig. 3b and c. At 200 °C, the yield stress difference obviously decreased (200 °C: 14 MPa; 20 °C: 83 MPa), while the strain hardening behavior of the ED sample and the TD sample was similar.

The above anisotropy variations at different tensile temperatures were shown more clearly in Fig. 3d by the  $\sigma_{ED} - \sigma_{TD}$  variations with the increase of logarithmic plastic strain. As shown, two aspects should be noted: with the increase of tensile temperature, the flow stress difference gradually decreased, and with the increase of logarithmic plastic strain, the flow stress difference first increased and then decreased, especially at 20 °C. The dynamic anisotropy evolution during tension deformation was closely related to the initial microstructure and the external deformation



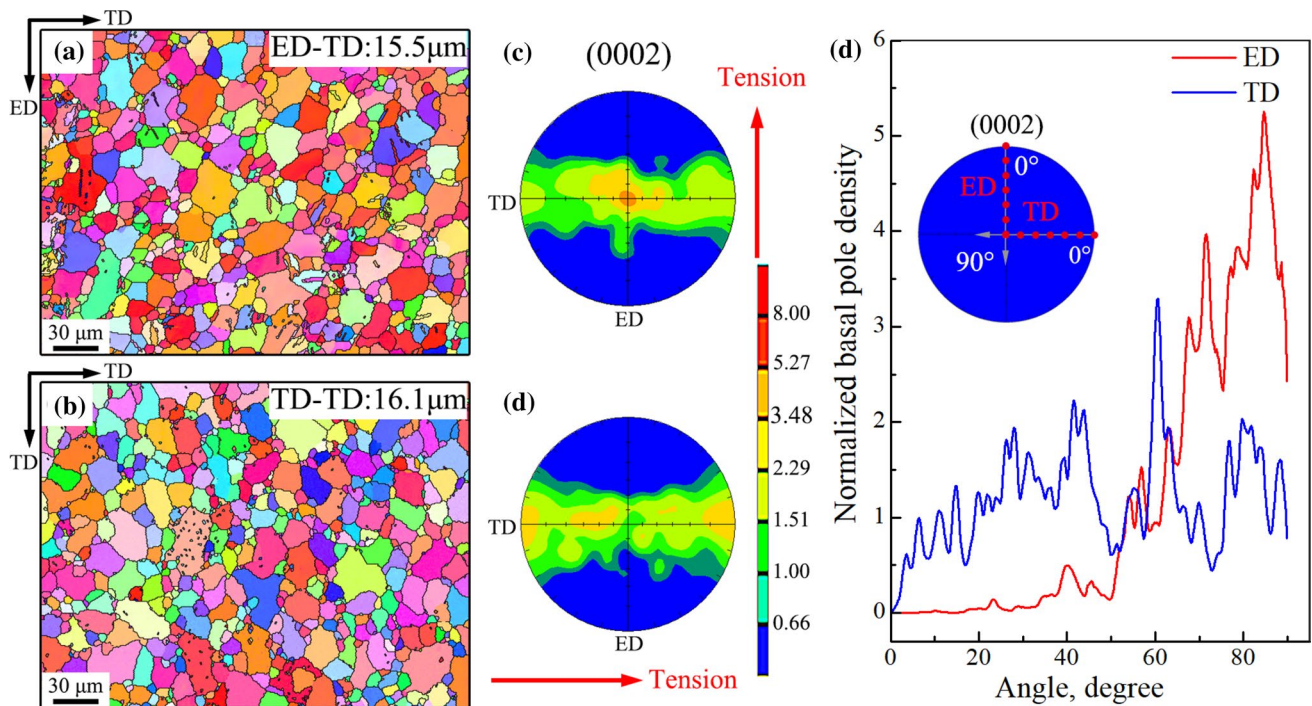


**Fig. 2** Microstructure characteristics and texture states of the initial material: inverse pole figure map **a** and (0002) pole figure **b** on the ED-TD plane sample; inverse pole figure map **c** and (0002) pole fig-

ure **d** on the TD-TD plane sample; (0002) pole density distributions along the ED and the TD **e**

conditions (strain and temperature in this work), which were described in the following sections.

In addition, Fig. 3a–c clearly showed that the square blue spots for the ED samples and the round red dots for the TD samples nearly approached their own experimental flow curves. This meant that the VPSC model accurately captured the tension deformation behaviors, and that the current material parameters ( $\tau^{0s}$ ,  $\tau^{1s}$ ,  $h^{0s}$ , and  $h^{1s}$ ) could be used to predict the texture evolutions and to determine the contribution of each deformation mode to the total strain. It should be noted that, although the initial material possessed the duplex microstructure, the prediction of the VPSC model was still reasonable, because this model applied the averaging method to solve the interaction between a given grain and a homogeneous matrix representing the rest of the material [31].

### 3.2 Microstructure Evolution Anisotropy

As reported, tension twinning was one key reason for the deformation behavior anisotropy of magnesium alloys [4, 11]. Its activation generally made the crystal lattice rotate by  $86.4^\circ$  around the  $\langle 11\text{--}20 \rangle$  axes with respect to the parent orientation. This promoted the formation of a tension twin boundary with a misorientation angle of  $86.4^\circ$ . This kind of boundary characteristic could be used here to identify the

activation of tension twinning during tension deformation, as shown in Fig. 4. The corresponding fractions of tension twin boundary were summarized in Fig. 4d. For the initial material, there existed some tension twin boundaries on the ED-TD plane ( $\sim 14\%$ ), whereas there were few on the TD-TD plane (only 2.9%, Fig. 4a). This difference was very likely attributed to the three-dimensional twin structure morphology. On the ED-TD plane, the lenticular twin morphology could be observed totally, while on the TD-TD plane, only the vertical projection of the twin boundary could be seen. The morphology of the tension twin boundary in Fig. 4 could validate such a hypothesis, in which the ED-TD plane exhibited the long tension twin boundary (red line) while the TD-TD plane exhibited the punctiform tension twin boundary (red dot). Here, the fraction of tension twin boundary for the initial material was expressed via the arithmetic mean of fractions from the ED-TD plane and from the TD-TD plane.

For the interruption tension samples, Fig. 4 depicted the large differences in the fraction of tension twin boundary. First, compared to the initial material, the fractions obviously decreased in the ED samples (Fig. 4b), but greatly increased in the TD samples (Fig. 4c). Second, increasing the tensile strain decreased the fraction of tension twin boundary for the ED samples and the TD samples simultaneously (e.g., the fractions for the TD samples from 17.4% at 0.1 to 9.5% at 0.2 under the temperature of  $20^\circ\text{C}$ ). Third,

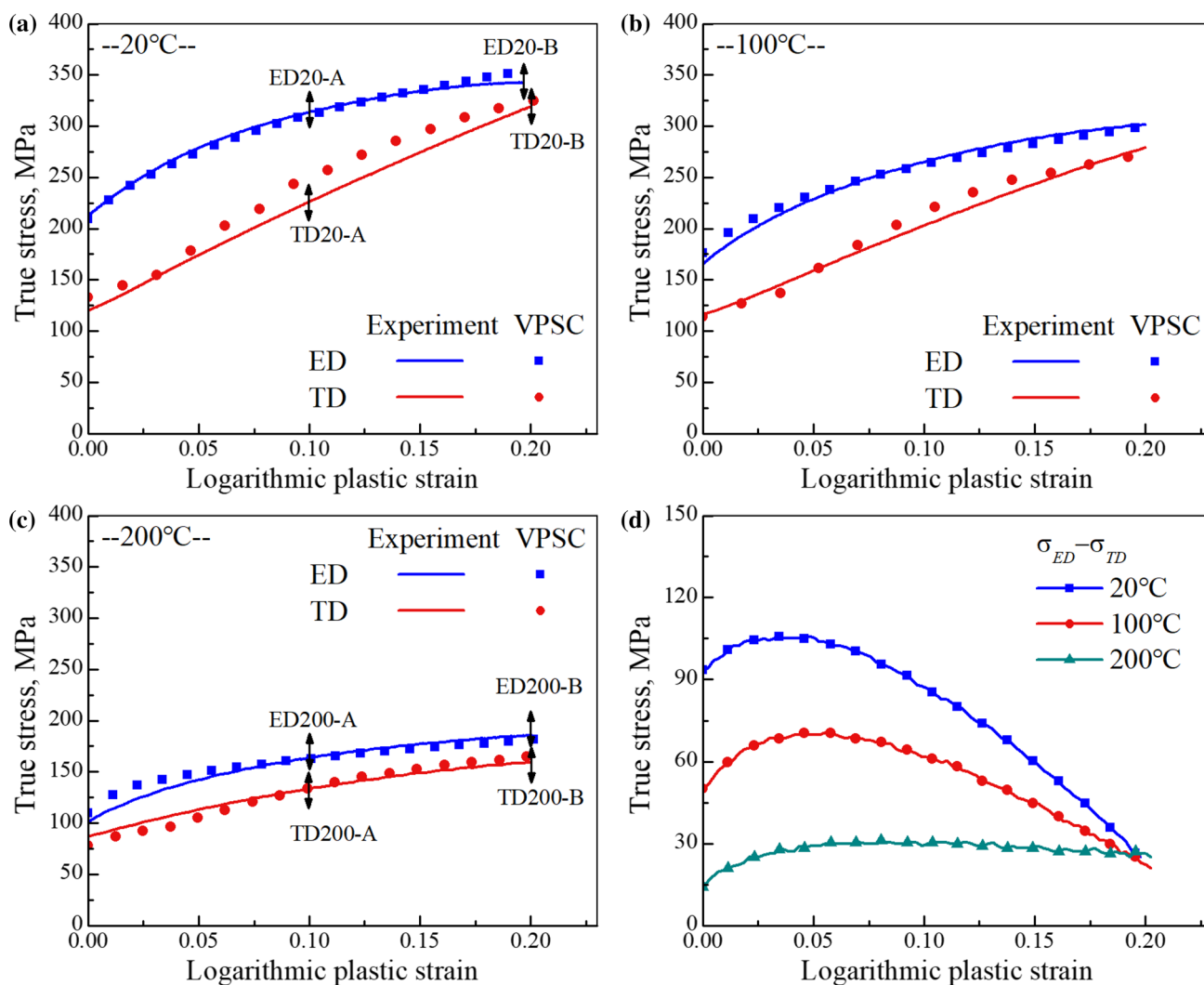


**Fig. 3** Experimental and VPSC predicted true stress—logarithmic plastic strain curves at deformation temperatures of **a** 20 °C, **b** 100 °C, **c** 200 °C, and the corresponding flow stress difference of  $\sigma_{ED} - \sigma_{TD}$  **d**

increasing the tensile temperature also decreased the fraction of tension twin boundary for the ED samples and the TD samples simultaneously (e.g., the fraction for the TD sample from 17.4% at 20 °C to 14.7% at 200 °C under the strain of 0.1).

Sahoo et al. suggested that twin nucleation was dependent on the strain concentration from adjacent grain, but its growth was mainly controlled by the crystal orientation of the parent grain [11]. Therefore, the appropriate grain orientation could effectively expand the tension twin region by twin boundary migration until the parent grain was consumed. For magnesium alloys, tension parallel to the c-axis and compression perpendicular to the c-axis, were two appropriate orientation relationships that trigger tension twinning [1, 26, 32]. As mentioned previously, the basal poles in the initial material spread diffusely along the TD, but they were nearly perpendicular to the ED (Fig. 2).

That was to say, the TD sample exhibited the appropriate orientation while the ED sample did not. Therefore, the tension deformation was more conducive to the tension twin growth for the TD samples than the ED samples. This made the tension twin boundary extend to the grain boundary easily in the TD samples but with difficulty in the ED samples [26], thereby producing a higher fraction of tension twin boundary in the TD samples. In addition, the continuous tension deformation caused inharmonious lattice rotation between the twin region and parent grain, severely destroying the exact tension twin misorientation angle of 86.4° [9, 11]. Such reaction was more obvious at the higher strain, and was deemed to be similar for the ED samples and TD samples because their tensile strains were the same. Therefore, their fraction difference of tension twin boundary decreased simultaneously with the increase



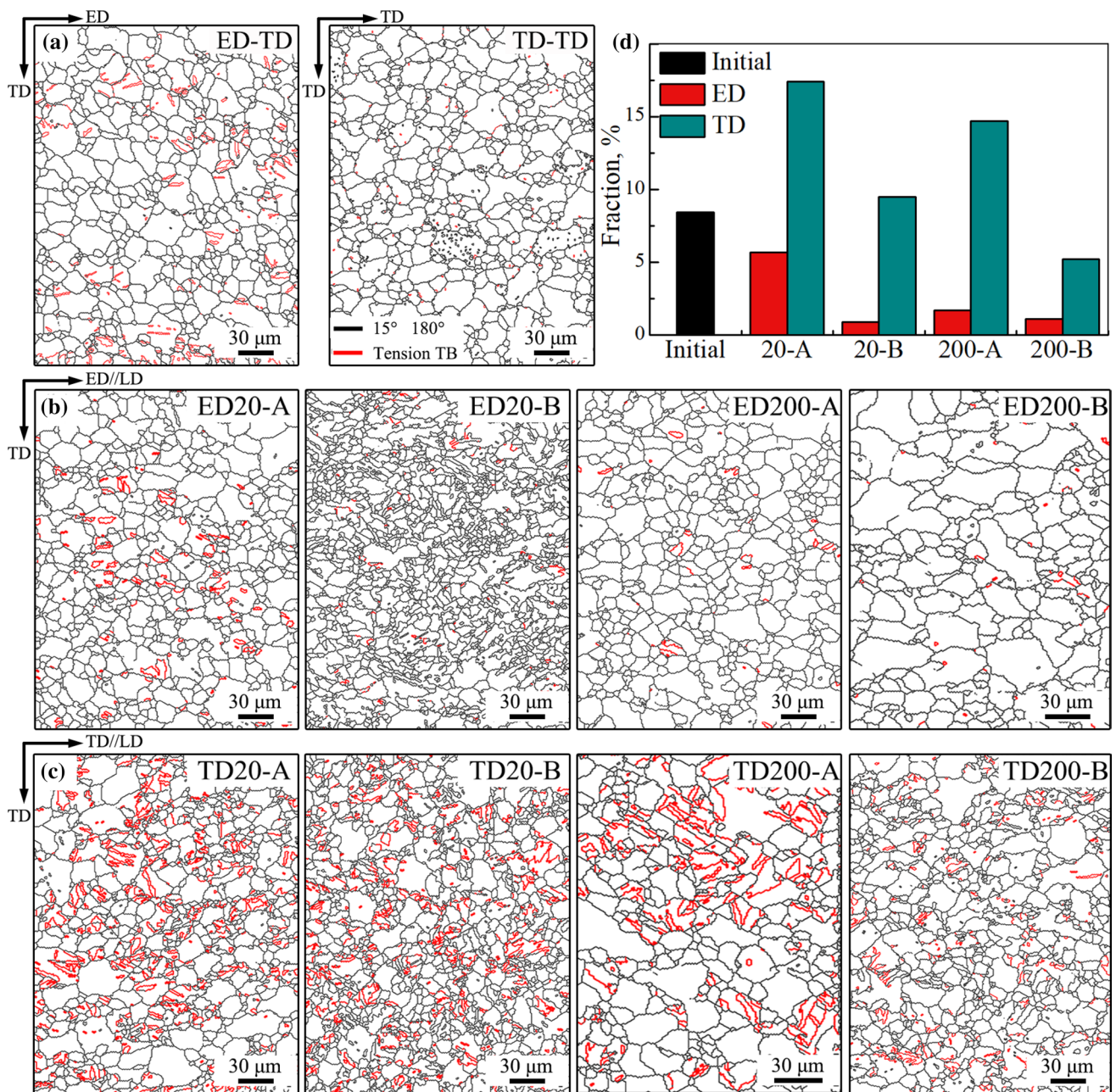


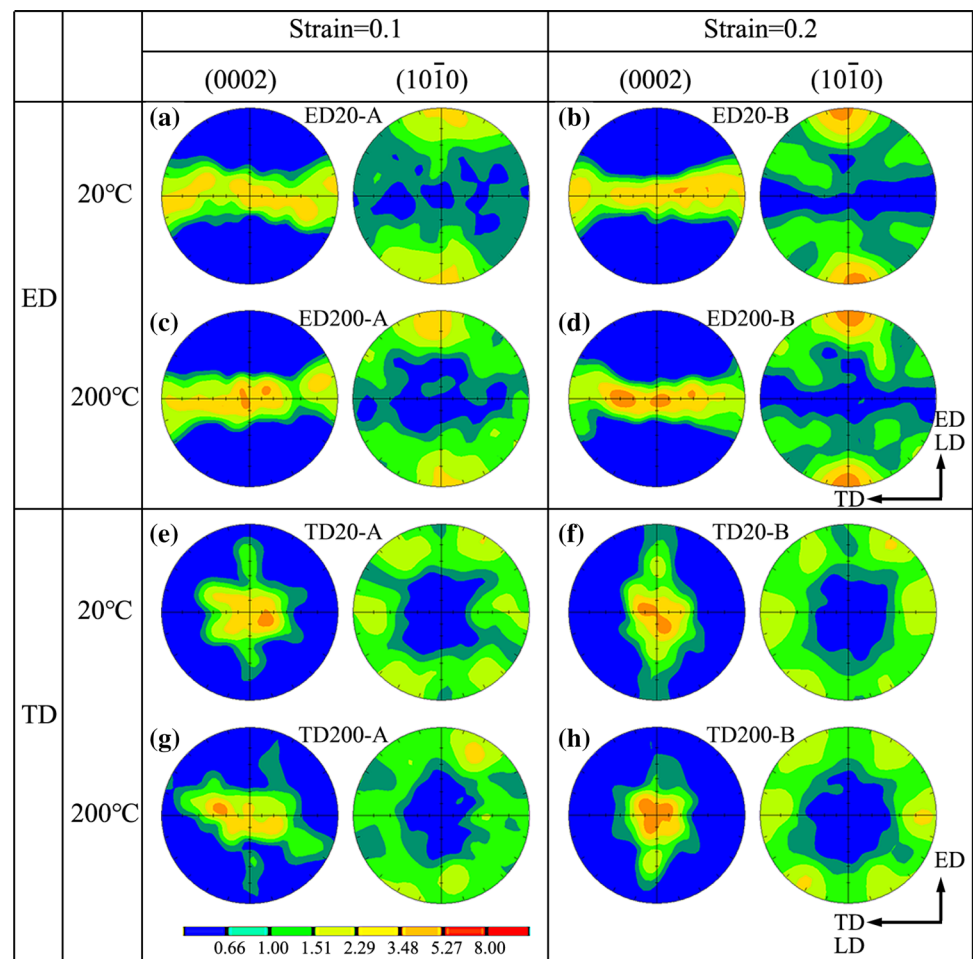
**Fig. 4** Microstructure characterizations via grain boundary misorientation map: **a** initial material on the ED-TD plane and the TD-TD plane; **b** ED samples; **c** TD samples; **d** the fractions of tension twin boundary under different tension conditions

of tensile strain. As described above, the twin nucleation was mainly influenced by the strain concentration from adjacent grains. In this work, the tension deformation at 200 °C relieved the strain concentration more easily owing to the strong effect of dynamic recovery (compared to the deformation at 20 °C). This reduced the propensity for tension twinning nucleation at 200 °C, and therefore produced a lower fraction of tension twin boundary.

### 3.3 Texture Evolution Anisotropy

Figure 5 depicted texture evolution using the (0002) and (10–10) pole figures for the ED samples and the TD samples under different tension conditions. As shown, all the ED samples in the (0002) pole figures exhibited a similar (0002)//ED-type texture in which most of the c-axes were perpendicular to the ED (Fig. 5a–d). Such (0002)//ED-type texture was consistent with the (0002)//LD-type texture because the LD was parallel to the ED. Instead, the texture

**Fig. 5** Experimental measured (0002) and (10–10) pole figures for different samples



variation in the (10–10) pole figures seemed more regular during tension deformation. Concretely, with the increase of tensile strain, a strengthened region in the (10–10) pole figures gradually developed along the LD where the texture intensity increased to 4.0 at 20 °C (ED20-B), and to 4.3 at 200 °C (ED200-B). This kind of texture state was generally described as the  $\langle 10\bar{1}0 \rangle$ //LD-type texture [11, 24, 27].

In comparison, the TD samples in the (0002) pole figures presented large variations under different tension conditions. The original c-axes parallel to the TD in the initial material (Fig. 2) disappeared and they rotated to the normal direction (ND) in the TD20-A sample at the strain of 0.1 and the temperature of 20 °C (Fig. 5e). Such rotations continued with the increase of tensile strain, causing the angle distributions of the c-axis away from the ND to narrow to  $\pm 45^\circ$  (TD20-B) from  $\pm 60^\circ$  (TD20-A) at the tensile strain of 0.2. As a result, the (0002) pole figure of the TD20-B sample (Fig. 5f) depicted a strong (0002)//TD-type texture in which most of the c-axes were perpendicular to the TD. Accordingly, the (0002)//TD-type texture could also be ascribed to the direction consistency of LD//TD. Similarly, the above c-axes rotations also occurred at the tensile temperature of 200 °C,

where the angular distributions of the c-axis away from the ND narrowed to  $\pm 50^\circ$  (TD200-B) from  $\pm 70^\circ$  (TD200-A). These results demonstrated that the tension deformation made more and more c-axes perpendicular to the TD.

Correspondingly, the VPSC model predicted similar texture evolutions for the ED samples and the TD samples (Fig. 6). As seen, three aspects were captured accurately by the VPSC model: (i) the gradually strengthened fiber texture in the ED samples with the increase of tensile strain in parts a–d of Fig. 6, (ii) the c-axes rotation trend from the TD to the ND in the TD samples with the increase of tensile strain in parts e–h of Fig. 6, and (iii) the development of  $\langle 10\bar{1}0 \rangle$ //LD-type texture in the ED samples and the TD samples. These texture evolution results again proved the accuracy of the VPSC prediction.

To further investigate the above texture evolutions for the ED samples and the TD samples, the activation fraction of each deformation mode during the tension deformation were extracted from the VPSC model, as shown in Fig. 7. Obviously, a large difference existed in the activation fraction of deformation mode between the ED samples and the TD samples. For the ED samples (Fig. 7a), the basal slips and



**Fig. 6** VPSC predicted (0002) and (10–10) pole figures for different samples

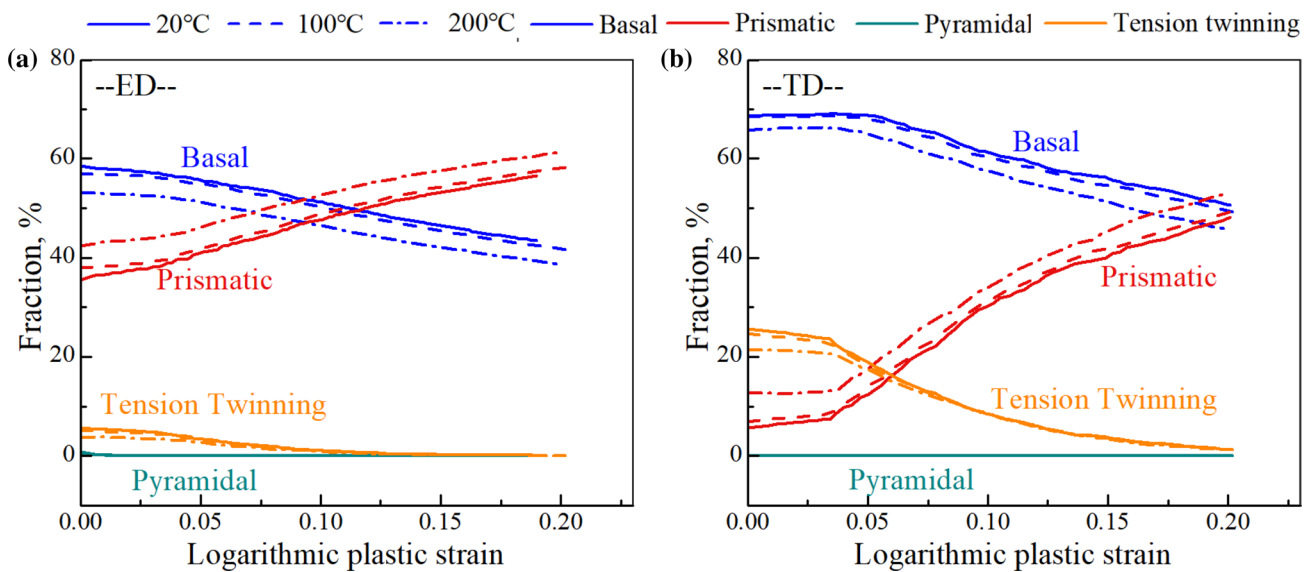
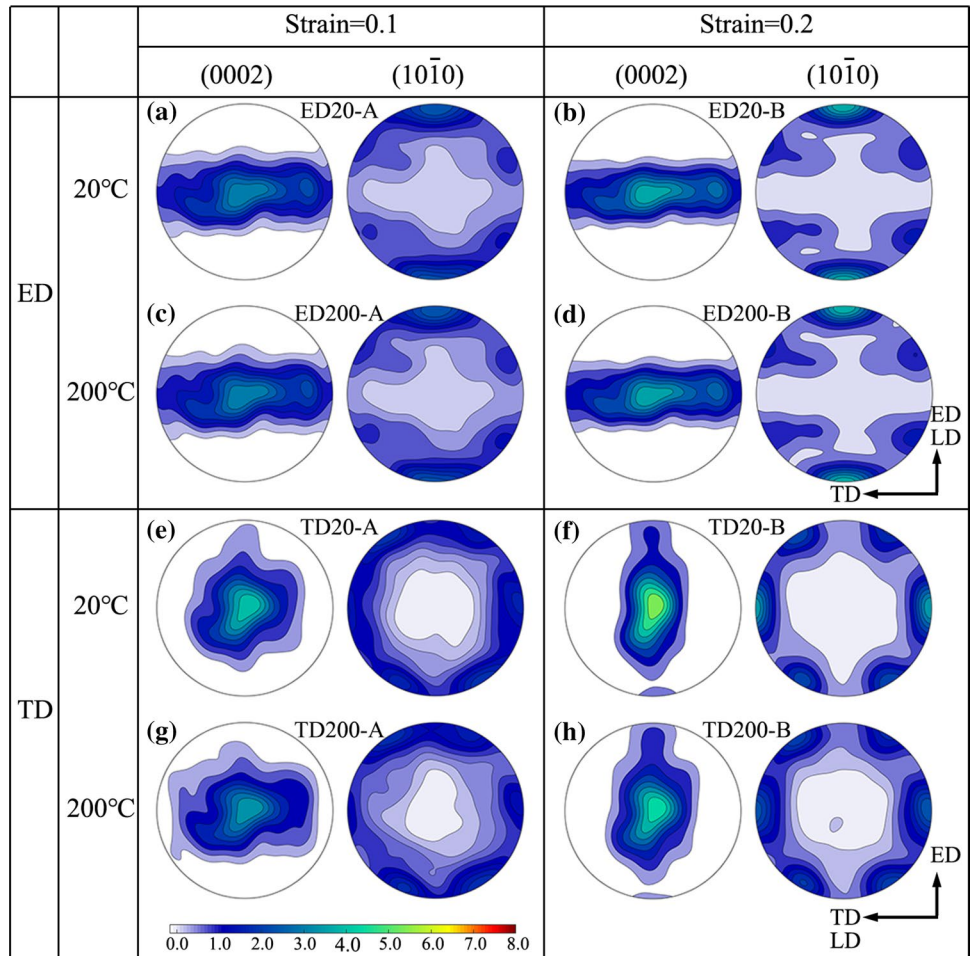


**Fig. 7** Relative activation fractions of each deformation mode predicted by the VPSC model as a function of logarithmic plastic strain

the prismatic slips were the deformation modes in the early stage of tension deformation, and the former was dominant. With the increase of tensile strain, the activation fraction of basal slip gradually decreased, while that of prismatic slip increased. Such variations continued during the entire tension deformation, and the activation fraction of prismatic slip exceeded the basal slip to become the predominant deformation mode at a specific plastic strain (0.11 at 20 °C, 0.1 at 100 °C, or 0.07 at 200 °C). It was recognized that whether a deformation mode was activated or not was mainly dependent on the ratio of CRSS to the Schmid factor ( $\sigma_0 = \tau_{CRSS}/m$ , where  $\sigma_0$ ,  $\tau_{CRSS}$ , and  $m$  are the activation stress, critical resolved shear stress, and Schmid factor, respectively. [8, 28]. According to the material parameters (Table 1), the CRSS of the basal slip was lowest. This made the basal slip activated more easily than the non-basal slip at the onset of tension deformation. However, with the increase of tensile strain, the activation of basal slip gradually rotated the basal plane toward a hard orientation, causing the decline of Schmid factor of the basal slip. Influenced by this, the activation stress of basal slip increased, and when it exceeded the activation stress of prismatic slip, extensive prismatic slips were activated and became the predominant deformation mode. These activations of deformation mode promoted the development of the tension-type texture in the ED samples. The activations of basal slips rotated their planes toward the ED (or LD), eventually strengthening the basal texture along the ED (or LD) and developing the (0002)//ED- or LD-type texture. At the same time, the crystal lattice would rotate around the  $\langle 0001 \rangle$  crystal direction due to the activation of prismatic slips and such rotation behavior promoted the development of  $\langle 10\bar{1}0 \rangle$ //LD-type texture [11, 24, 27].

In comparison, the deformation modes for the TD samples in Fig. 7b were basal slip and tension twinning at the onset of tension deformation. The activation of tension twinning agreed well with the tension twin boundaries in Fig. 4c. As described above, when the tension direction was the TD, the initial material exhibited some grains of which the orientation met the activation condition of tension twinning during tension deformation (tension parallel to the c-axis). However, with the increase of tensile strain, the crystal rotation weakened the Schmid factor advantage of basal slip and tension twinning as well, subsequently decreasing their activation fractions. Instead, owing to the geometric hardening of the basal slip and tension twinning, the activation stress of prismatic slips became relatively lower. As a result, the prismatic slips were activated, and formed an increased trend of activation fractions (Fig. 7b). Similarly, the tension texture for the TD samples was also attributed to the activation of each deformation mode. According to Hong's study, when the tension direction was parallel to the c-axis, six (10–12) tension twin variants tended to be activated and these induced the crystallographic lattice reorientation of

86.4° [29]. This made the c-axis rotate toward the direction perpendicular to the TD (LD), developing the texture component with a spread of basal poles along the ED. For the basal slips, their activations also rotated the basal planes toward the loading direction which was TD instead of ED here, and thus the (0002)//TD- or LD-type texture component developed. By superposition of the texture components induced by the basal slip and the tension twinning, the (0002)//TD- or LD-type texture developed and would be obviously strengthened with the increase of tensile strain. Of course, the activations of prismatic slip also made the  $\langle 10\bar{1}0 \rangle$  rotate to the tension loading direction (TD), further developing the  $\langle 10\bar{1}0 \rangle$ //TD- or LD-texture component in the TD samples [11, 24, 27].

Additionally, it could be seen in Fig. 7 that increasing the tensile temperature decreased the activation fractions of basal slip and tension twinning, but increased the activation fractions of prismatic slip. This was mainly ascribed to the ratio decline of the CRSS for the non-basal slip to that for the basal slip and tension twinning with the increase of tensile temperature [15]. Actually, each deformation mode exhibited hardening behavior during plastic deformation, which could be described according to the Voce hardening (Eq. 3) in VPSC model. Combining the material parameters in Table 1 and Eq. 3, the CRSS of each deformation mode under each different tension condition was calculated, as shown in Fig. 8 and summarized in Table 2. Clearly, increasing the tensile strain hardened the CRSS of each deformation mode, especially the prismatic slip and pyramidal slip (Fig. 8a–c). However, with the increase of tensile temperature, the CRSS of prismatic slip and pyramidal slip decreased, while that of the basal slip and tension twinning was almost unchanged. As a result, the CRSS ratio of the basal slip: tension twinning: prismatic slip: pyramidal slip changed to 1:1.9:5.1:7.7 at 200 °C from 1:1.6:8.6:12.9 at 20 °C, when the strain was zero (Fig. 8d). Other tensile strain conditions also exhibited similar variations (strain = 0.1 and 0.2). Such variations meant that the contribution of prismatic slip to the total strain increased while that of basal slip decreased. That was to say, the degree of crystal rotation caused by the basal slip was weakened at the higher tensile temperature, thereby developing a weak basal texture more easily compared to the lower tensile temperature (Figs. 5 and 6).

### 3.4 Tension Deformation Behavior Anisotropy

As described above, the entire tension deformation behavior exhibited the large anisotropy between the ED sample and the TD sample, but such anisotropy gradually decreased with the increase of the tensile temperature or the tensile strain (Fig. 3). For the polycrystalline magnesium alloys, the anisotropy of the tension deformation behavior involved strain hardening behavior and

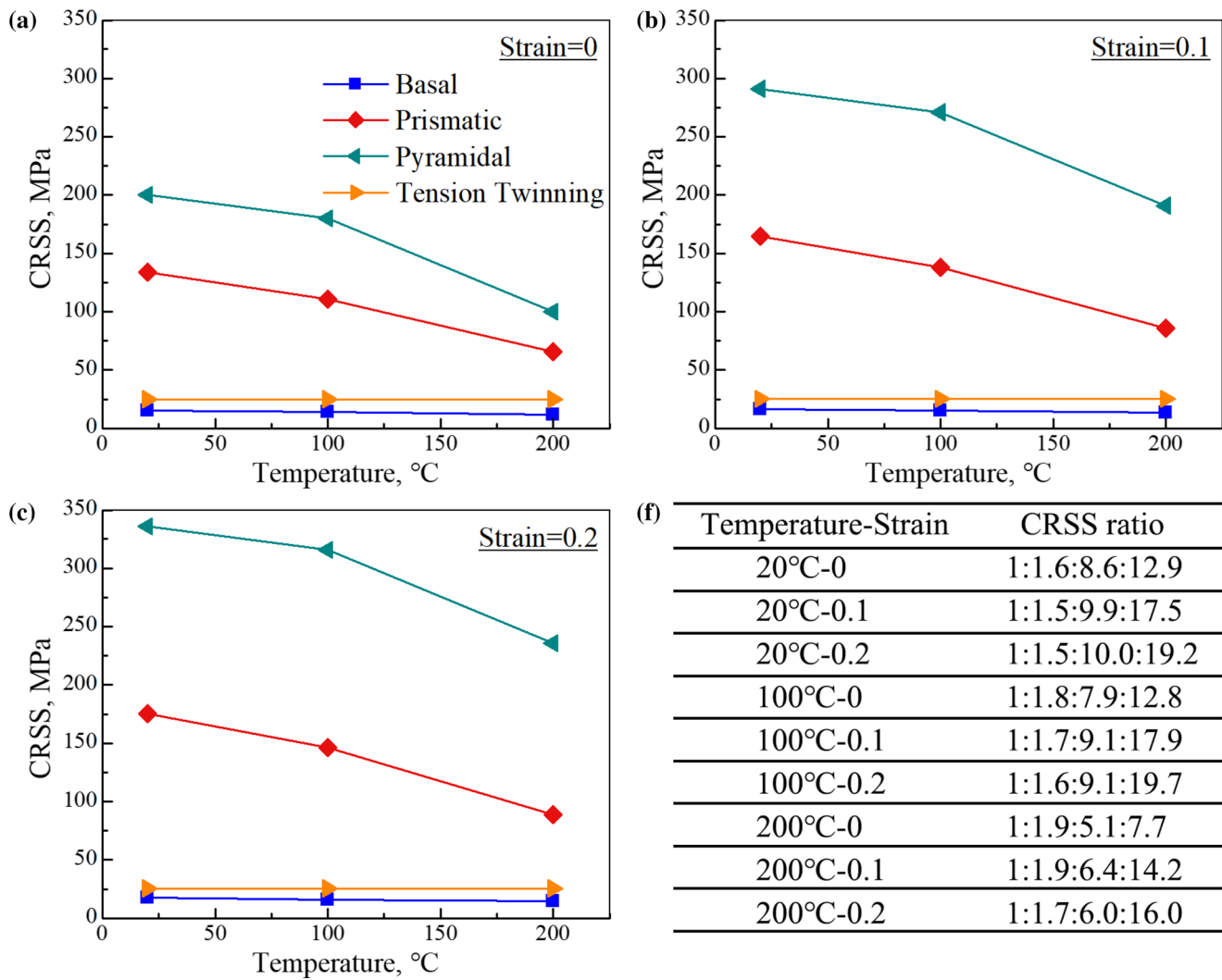


**Fig. 8** The CRSS variations of each deformation mode as a function of tensile temperatures for **a** strain=0, **b** strain=0.1 and **c** strain=0.2, and **d** the corresponding CRSS ratio (Basal slip: Tension twinning: Prismatic slip: Pyramidal slip)

**Table 2** The CRSS of each deformation mode at different tension conditions (unit: MPa)

Temperature (°C)	Strain	Basal	Prismatic	Pyramidal	Tension twinning
20	0	15.6	134.6	200.0	25.0
	0.1	16.5	164.5	290.9	25.2
	0.2	17.5	175.0	335.6	25.4
100	0	14.1	110.7	180.0	25.0
	0.1	15.1	138.1	270.9	25.2
	0.2	16.0	146.3	315.7	25.4
200	0	12.2	65.7	100.0	25.0
	0.1	13.7	85.6	190.7	25.2
	0.2	14.7	88.6	235.5	25.4

was closely related to the texture [9]. The effect of texture on the deformation behavior could be expressed by the Taylor law ( $\sigma = M\tau^{\text{ref}}$ ) where  $\sigma$ ,  $M$ , and  $\tau^{\text{ref}}$  were the flow stress, Taylor factor, and reference shear stress representing the macroscopic average resolved shear stress, respectively [9, 28, 30]. Therefore, to clarify the above tension deformation behavior anisotropy between the ED sample and the TD sample, the Taylor factor ( $M$ ) and the macroscopic average resolved shear stress ( $\tau^{\text{ref}}$ ) should be characterized in detail. Here, the Taylor factors for the ED samples and the TD samples under different tension conditions were calculated according to the experimental EBSD data, as shown in Table 3. As seen, the Taylor factors of the ED samples were slightly higher than those of the TD samples, but importantly, all the Taylor factor ratios ( $M_{\text{ED sample}}/M_{\text{TD sample}}$ ) were close to one. This meant that the above obvious tension deformation behavior

**Table 3** Calculated Taylor factor  $M$  under different tension conditions. ( $M_{ED\ sample}$  and  $M_{TD\ sample}$  are the Taylor factors for the ED samples and the TD samples, respectively;  $M_{ratio}$  is the Taylor factor ratio using  $M_{ED\ sample}/M_{TD\ sample}$ )

State	20 °C-0.1	20 °C-0.2	200 °C-0.1	200 °C-0.2
$M_{ED\ sample}$	2.6052	2.6073	2.5876	2.5986
$M_{TD\ sample}$	2.5575	2.5676	2.5667	2.5776
$M_{ratio}$	1.0186	1.0154	1.0081	1.0081

anisotropy between the ED samples and the TD samples was probably not attributable to the Taylor factor difference. Therefore, the macroscopic average resolved shear stress should be specifically considered.

The current tension deformation involved various deformation modes instead of a single deformation mode. For such cases of multiple slip activations, the macroscopic average resolved shear stress should be estimated considering the CRSS of each deformation mode and their respective contributions to the total deformation strain. The previous descriptions presented the hardening behavior of each deformation mode and the CRSS of each deformation mode under different tension conditions (Table 2). In this work, the macroscopic average resolved shear stress (reference shear stress) was quantified using the weighted-average method in which the CRSS of each deformation mode was multiplied by its respective activation fraction. Figure 9a showed the calculated reference shear stresses under different tension conditions. Obviously, the reference shear stresses for both the ED samples and the TD samples gradually decreased with the increase of tensile temperature, whereas these stresses increased with the increase of tensile strain. Under the same tension condition, the reference shear stresses were higher in the ED samples than in the TD samples. However, with the increase of tensile strain, the reference shear stresses in the TD samples increased more obviously than those in the ED samples. Importantly, this caused the difference variations of reference shear stress between the ED samples and the TD samples. Such difference variations in this work were characterized by the ratios ( $Ratio = \tau_{ref}^{ED} / \tau_{ref}^{TD}$ ), as shown in Fig. 9b. It could be seen that increasing the tensile strain, significantly decreased the difference ratio. Concretely, the difference ratio decreased to 1.13 (strain = 0.2) from 2.37 (strain = 0) at 20 °C, to 1.13 (strain = 0.2) from 2.20 (strain = 0) at 100 °C, and to 1.11 (strain = 0.2) from 1.65 (strain = 0) at 200 °C. Besides, with the increase of tensile temperature, the difference ratio also exhibited a decline trend. The key point was that the difference ratio of reference shear stress varied more obviously than the Taylor factor ratio difference. Therefore, the difference in the reference shear stress between

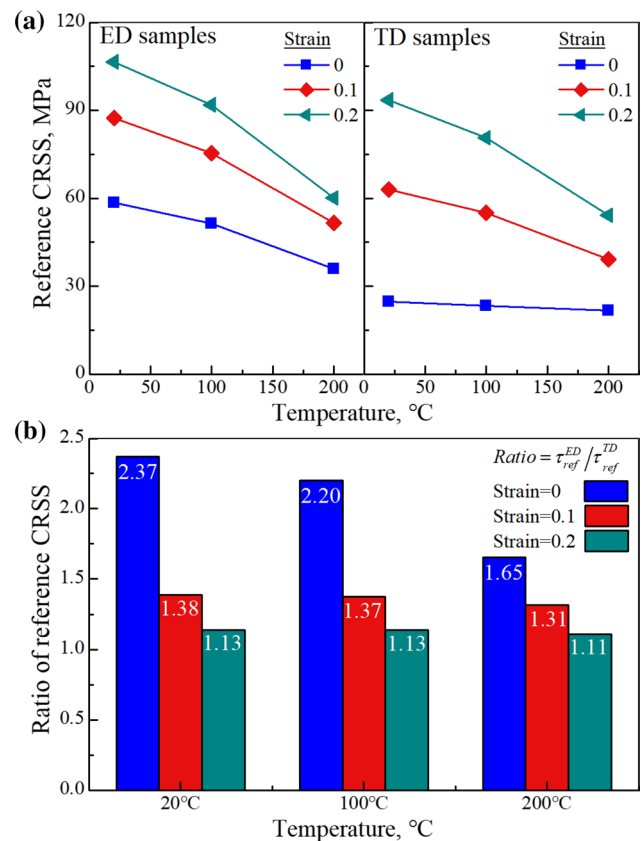


**Fig. 9** The calculated reference shear stress as a function of the tensile temperature **a**, and the corresponding difference ratios of reference shear stress **b**

the ED sample and the TD sample was the key factor causing the tension deformation behavior anisotropy.

In essence, the reference shear stress was closely related to the activation of each deformation mode. At the onset of tension deformation, the activation fraction of tension twinning was lower in the ED samples than in the TD samples, which was clearly shown in Figs. 4 and 7. During the tension deformation of ED sample, the tensile strain needed to be accommodated by activation of the non-basal slips, because a single basal slip could not meet the requirement of homogeneous deformation according to the Von Mises criterion, and meanwhile could not accommodate the c-axis strain [5]. However, owing to the high CRSS of non-basal slips, the external stresses had to be high enough to produce plastic deformation behavior, thereby presenting the higher flow stress and higher reference shear stress. In contrast, the activation of tension twinning in the TD samples not only could accommodate the c-axis but could also produce the plastic deformation behavior under lower external stress due to its lower CRSS [4]. This resulted in the TD samples possessing the lower flow stress and lower reference shear stress at the onset of tension deformation. In further comparison of



the higher flow stress in the ED samples, the large tension deformation behavior anisotropy developed at the onset of tension deformation. With the increase of tensile strain, the strain hardening behavior was obvious in the ED sample owing to its multi-slip mechanism, while that changed little in the TD sample. As a result, the anisotropy exhibited an amplification stage in Fig. 3d. However, with the consumption of tension twinning in the TD samples, the deformation mechanism gradually transformed to the multi-slip mechanism from the tension twinning. At this moment, the rapid hardening ability in the tension twin region, and the hardening ability of the multi-slip mechanism in the matrix region, together contributed to strain hardening in the TD samples. Consequently, their flow stresses improved and this narrowed the difference in tension deformation behavior [16]. In term of the tensile temperature, its increase weakened the CRSS difference between the basal slip and non-basal slip, making the non-basal slip easily activated. Further, this gave rise to similar reference shear stresses between the ED samples and the TD samples (Fig. 9a), thus presenting similar tension deformation behavior. In essence, the crystalline structure symmetry of the magnesium alloys increased at the higher tensile temperature, making their deformation behavior similar to the aluminum alloys that exhibited isotropic material.

## 4 Conclusions

In this work, the anisotropy variation of the tensile flow stress of as-extruded AZ31 magnesium alloy was investigated under various tensile strains and tensile temperatures by combining the experimental and VPSC model results. The main conclusions were as follows.

1. The anisotropy of the flow stress obviously decreased with increase of the tensile temperature, but with increase of the tensile strain, such anisotropy first increased and subsequently decreased.
2. The VPSC results and the tension twin boundary results, together revealed that the activation difference between the non-basal slips and the tension twinning at the onset of tension deformation caused the increased stage of tension deformation anisotropy.
3. The (0002)//LD-type texture was developed due to activation of the basal slip, and is strengthened when the tension twinning is activated. The activation of the prismatic slip produces the  $\langle 10\text{--}10 \rangle$ //LD-type texture.
4. The macroscopic average resolved shear stress calculated according to the critical resolved shear stress of each deformation mode and their respective activation fractions, was the major reason for the decline of tension

deformation behavior anisotropy compared to the Taylor factors.

**Acknowledgements** This work was supported by National Natural Science Foundation of China (Grant Nos. 51975146, 51801139), Natural Science Foundation of Shandong Province (Grant Nos. ZR2020QE171, ZR2021ME073), Key Research and Development Plan in Shandong Province (Grant No. 2019JZZY010364). This work was supported by the National Research Foundation of Korea (NRF) grant funded by the Korea government (MSIP) (NRF-2021R1A2C3006662).

## Declarations

**Conflict of interest** The authors declare that they have no known competing financial interests or personal relationships that could have appeared to influence the work reported in this paper.

## References

1. S.A. Habib, A.S. Khan, T. Gnäupel-Herold, J.T. Lloyd, S.E. Schoenfeld, *Int. J. Plasticity* **95**, 163 (2017)
2. J. Xie, J. Zhang, Z. You, S. Liu, K. Guan, R. Wu, J. Wang, J. Feng, *J. Magnes. Alloy.* **9**, 41 (2021)
3. C.S. Hyun, M.S. Kim, S.H. Choi, K.S. Shin, *Acta Mater.* **156**, 342 (2018)
4. D.D. Yin, C.J. Boehlert, L.J. Long, G.H. Huang, H. Zhou, J. Zheng, Q.D. Wang, *Int. J. Plasticity* **136**, 102878 (2021)
5. L. Hu, H. Lv, L. Shi, Y. Chen, Q. Chen, T. Zhou, M. Li, M. Yang, *J. Magnes. Alloy.* (2021). <https://doi.org/10.1016/j.jma.2020.12.008>
6. J.W. Park, K.S. Shin, *Mater. Sci. Eng. A* **688**, 56 (2017)
7. J.W. Park, S.J. Park, K.S. Shin, *Met. Mater. Int.* **23**, 444 (2017)
8. B. Guan, Y. Xin, X. Huang, P. Wu, Q. Liu, *Acta Mater.* **173**, 142 (2019)
9. S.K. Sahoo, L.S. Toth, S. Biswas, *Int. J. Plasticity* **119**, 273 (2019)
10. A. Chapuis, Q. Liu, *Mater. Sci. Eng. A* **725**, 108 (2018)
11. Y.Q. Chai, C.J. Boehlert, Y.F. Wan, G.H. Huang, H. Zhou, J. Zheng, Q.D. Wang, D.D. Yin, *Metall. Mater. Trans. A* **52**, 449 (2021)
12. Z. Li, G. Zhou, D. Li, M.K. Jain, Y. Peng, P. Wu, *Int. J. Plasticity* **135**, 102822 (2020)
13. N. Dixit, K.Y. Xie, K.J. Hemker, K.T. Ramesh, *Acta Mater.* **87**, 56 (2015)
14. S.R. Agnew, J.A. Horton, T.M. Lillo, D.W. Brown, *Scripta Mater.* **50**, 377 (2004)
15. W. Wang, W. Chen, W. Zhang, G. Cui, E. Wang, *J. Mater. Sci. Technol.* **34**, 2042 (2018)
16. P.D. Wu, X.Q. Guo, H. Qiao, S.R. Agnew, D.J. Lloyd, J.D. Embury, *Acta Mater.* **122**, 369 (2017)
17. A. Molinari, G.R. Canova, S. Ahzi, *Acta Metall.* **35**, 2983 (1987)
18. R.A. Lebensohn, C.N. Tomé, *Mater. Sci. Eng. A* **175**, 71 (1994)
19. R.A. Lebensohn, C.N. Tomé, *Acta Metall.* **41**, 2611 (1993)
20. F. Kabirian, A.S. Khan, T. Gnäupel-Herold, *Int. J. Plasticity* **68**, 1 (2015)
21. W. Ren, R. Xin, J. Xu, B. Song, L. Zhang, Q. Liu, *J. Alloy. Compd.* **792**, 610 (2019)
22. C.N. Tomé, R.A. Lebensohn, U.F. Kocks, *Acta Metall. Mater.* **39**, 2667 (1991)
23. L. Hu, S. Jiang, Y. Zhang, *Metals* **7**, 356 (2017)

24. W. Wang, G. Cui, W. Zhang, W. Chen, E. Wang, *Mater. Sci. Eng. A* **724**, 486 (2018)
25. W. Wang, L. Ma, S. Chai, W. Zhang, W. Chen, Y. Feng, G. Cui, *Mater. Sci. Eng. A* **730**, 162 (2018)
26. Y. Cheng, Y. Fu, Y. Xin, G. Chen, P. Wu, X. Huang, Q. Liu, *Int. J. Plasticity* **132**, 102754 (2020)
27. A. Imandoust, C.D. Barrett, A.L. Oppedal, W.R. Whittington, Y. Paudel, H. El Kadiri, *Acta Mater.* **138**, 27 (2017)
28. Y. Wang, H. Choo, *Acta Mater.* **81**, 83 (2014)
29. S.-G. Hong, S.H. Park, C.S. Lee, *Acta Mater.* **58**, 5873 (2010)
30. H. Yu, Y. Xin, M. Wang, Q. Liu, *J. Mater. Sci. Technol.* **34**, 248 (2018)
31. H. Wang, P.D. Wu, C.N. Tomé, J. Wang, *Int. J. Solids Struct.* **49**, 2155 (2012)
32. R. Ni, Z.W. Jiang, D.D. Yin, W. Yang, H. Zhou, J. Zheng, Q.D. Wang, *Metall. Mater. Trans. A* **53**, 535 (2022)
33. X. Li, B. Jiang, J. He, J. Zhang, Z. Jiang, B. Liu, F. Pan, *J. Alloy. Compd.* **721**, 106 (2017)
34. H. Zhang, G. Huang, D. Kong, G. Sang, B. Song, *J. Mater. Process. Tech.* **211**, 1575 (2011)

**Publisher's Note** Springer Nature remains neutral with regard to jurisdictional claims in published maps and institutional affiliations.